


Design of a rapid-cycling synchrotron for flash proton therapy

Ying Shi ^{1,2}, Man-Zhou Zhang ^{1,2,3,*}, Lian-Hua Ou-Yang ^{1,2,3}, Zhi-Ling Chen ^{1,2,3}, Xiu-Fang Li³ and De-Ming Li^{1,2,3}

¹Shanghai Institute of Applied Physics, Chinese Academy of Sciences, Shanghai 201800, China

²University of Chinese Academy of Sciences, Beijing 100049, China

³Shanghai Advanced Research Institute, Chinese Academy of Sciences, Shanghai 201210, China

The purpose of this study was to design a rapid cycling synchrotron, making it capable of proton beam ultra-high dose rate irradiation, inspired by laser accelerators. The design had to be cheap and simple. We consider our design from six aspects: the lattice, injection, extraction, space charge effects, eddy current effects and energy switching. Efficiency and particle quantity must be addressed when injected. The space charge effects at the injection could affect particles' number. The eddy current effects in the vacuum chambers would affect the magnetic field itself and generate heat, all of which need to be taken into account. Fast extraction can obtain 10^{10} protons/pulse, equal to instantaneous dose rate up to 10^7 Gy/s in a very short time, while changing various extraction energies rapidly and easily to various deposition depths. In the further research we expect to combine a delivery system with this accelerator to realize the FLASH irradiation.

Keywords: FLASH, Rapid-cycling Synchrotron, Proton therapy

I. INTRODUCTION

Radiotherapy aims to deliver a tumoricidal dose to eradicate tumors while reducing damage to the surrounding normal tissue. For decades, radiotherapy has been improved by using novel technologies, one of which is FLASH. In FLASH radiation therapy, single short treatment pulses shorter than 500 ms are delivered at ultrahigh average dose rates exceeding 40 Gy/s, significantly exceeding the commonly used average dose rates of approximately 0.05 Gy/s.

The FLASH effect was originally reported in the 1960s, although further investigations were largely halted due to logistical difficulties in translating the findings into clinical practice. In 2014, a well-established lung-fibrosis model using C57BL/6J mice was presented as the first proof-of-principle study [1]. Doses of up to 30 Gy were delivered in two ways: a single dose > 40 Gy/s in FLASH mode and < 0.03 Gy/s in conventional (CONV) mode. The results demonstrated a complete lack of acute pneumonitis and late lung fibrosis after bilateral thoracic irradiation of mice with FLASH at doses known to trigger the development of pulmonary fibrosis in 100% of the animals after CONV irradiation. FLASH radiotherapy consistently widens the therapeutic window with better sparing of normal tissue. Their potential for clinical applications has attracted significant interest from the medical community. However, the radiobiology of FLASH radiation therapy remains unclear. In most studies, this has been explained based on oxygen depletion, free radical production/recombination, inter-track effects, and sparing of the immune system [2, 3].

Subsequent research was undertaken at Lausanne University Hospital and Stanford University School of Medicine to ascertain if the same effect is observed for object recognition ability in mice after brain irradiation and for long-term memory deficits in these animals. The results of these inves-

tigations proved to be encouraging [4–6]. Ultra-high dose-rate irradiation showed better preservation of zebrafish embryos at all doses when compared to conventional irradiation. Additionally, the experiments demonstrated that the higher the dose rate, the better the growth of zebrafish embryos was preserved. Moreover, variations in the frequency and adjustments in the pulse width during FLASH radiation did not negatively impact the growth of the embryos [6–8]. Research on cats and minipigs has also shown positive biological effects [9]. In 2019, a 15 Gy FLASH-RT dose was administered for 90 ms to one of the most resistant and progressive skin lesions with a diameter of 3.5 cm. The skin reaction was minimal when compared to earlier conventional radiation [10].

FLASH is mainly effective for three types of tumors: radioresistant tumors requiring increased doses, recurrent tumors requiring re-radiotherapy with preservation of normal tissues, and normal tissues with high radiosensitivity. An assumption underlying several FLASH treatment planning studies is that there is no dose threshold for FLASH-sparing effects [11–14]. However, in further studies, a dose threshold between 5 and 10 Gy must be considered [15–18]. Therefore, further biological research is required to determine whether a dose threshold triggers FLASH effects.

Most studies have used electron beams with low tissue penetration, limiting their application in clinical practice. A promising alternative to the FLASH delivery method is proton beam therapy, which can offer superior dose distribution within the tissue. Although many experiments using proton FLASH have been conducted, to date, they have been limited to small volumes or shooting through [19]. There are many technological challenges in proton FLASH such as higher beam currents, dose monitoring, and beam modulation.

Given the limitations of the stored particle number and energy change time, traditional synchrotron-based proton therapy is not suitable for FLASH irradiation. The former requires large synchrotrons and a higher injection energy. The 3D ridge filter can remove the energy change time. Currently, laser plasma researchers have proposed another approach to achieving FLASH therapy: very high instantaneous dose rate,

* Corresponding author, zhangmanzhou@sinap.ac.cn

up to 10^9 Gy/s for less than nano seconds, but low average dose rate 1Gy/s also shows FLASH effect [20–25]. Compared to the laser plasma accelerator, the rapid cycling synchrotron is a simpler, cheaper, and more realistic way to provide this type of dose rates. In this study, we present a design of the rapid cycling medical synchrotron (RCMS) for proton cancer therapy facilities. The RCMS can provide several 10^{10} protons/pulse with the advantages of small beam envelopes and a narrower inner diameter of the vacuum chamber. The repetition rate was as high as 25 Hz, and it was easy to change the energy of each spill.

II. MAIN RCS PARAMETERS

A. Dose rate and accelerator types

The ability to provide a dose of 2 Gy in a volume of 1 liter is a common clinical criterion for proton therapy. This equates to 1.9×10^{11} protons for a cube of $10\text{ cm} \times 10\text{ cm} \times 10\text{ cm}$ at a depth of 10–20 cm in water at 2 Gy. For the FLASH treatment, 4 Gy (3.8×10^{11} protons) delivered within approximately 100 ms corresponds to a current of 600 nA or an average dose rate of 40 Gy/s [26]. With current medical accelerator technology, only isochronous cyclotrons can generate such high continuous beam currents.

Cyclotrons are the most often used accelerators in proton therapy. A cyclotron generates a high-intensity continuous beam at a fixed energy. To obtain the required energy, it must use a degrader. To modify the required energy, the degrader adjusts the physical thickness or the inserted degrader material. If there is a need for a quick shift in accelerator energy, the degrader is required to change beam energy in several tens of millisecond. But shorter than 0.1 ms/energy step is a significant challenge. At the same time, when the beam travels through the degrader, scattering and ionization losses occur, resulting in an increase in the beam emittance and energy spread, especially at low energies [27, 28]. For FLASH therapy, 3D ridge filter is used to avoid energy change [26].

The Linac accelerator exhibits the advantages of a higher peak current and smaller beam emittance. New linac designs have a sufficiently short time to modify the beam energy from pulse to pulse [29–31]. When it comes to true, it may realize complete spot scanning in the clinic. The enormous size and expensive price of linac are also factors to consider [1, 5].

A slow-cycling synchrotron can preselect the extracted energy, eliminating the need for a degrader. Its whole cycle comprising of the injection, ramping up, extraction and subsequent return of the magnetic field, takes a few seconds. Considering this duration, the typical synchrotron usually operates at a low injection energy, resulting in a small space-charge limit. Generally, slow-cycling synchrotrons deliver a lower average and instantaneous dose to patients [4, 32].

Several studies have been conducted on the laser-plasma acceleration of proton beams [25, 33]. Researchers have frequently combined ultrathin targets with beam optics to realize the transmission of several Gys in nanoseconds. In terms of clinical applications, some challenges, such as the maximum

energy and intensity of the proton beams, low repetition rate, quality assurance, patient safety, control, and repeatability of the laser pulse output, remain to be addressed. Although proton laser plasma acceleration, to date, is not available for therapeutic use, it provides a new way to achieve FLASH therapy. Inspired by laser plasma researchers, we can use a very high instantaneous dose rate with a low average dose rate to realize the FLASH effect.

The rapid-cycling synchrotron shares similar beam characteristics with the laser plasma accelerator, but it exhibits much higher beam energy and intensity. We plan to design an RCMS capable of providing 10^{10} protons/pulse at a repetition rate of 25 Hz. This equates to 2.5×10^{11} protons/s, slightly more than 60 Gy in 1 min in one liter of volume, with the mean dose rate of approximately 1 Gy/s. But the length of a beam pulse is only a few tens nano-seconds. If we can change beam energy from pulse to pulse and for scattering method that means several Gys for a energy slice, the instantaneous dose rate is more than 10^7 Gy/s. For scanning method, this means a spot requires a pulse, and the instantaneous dose rate is up to 10^9 Gy/s, but the dose control is very difficult.

B. The lattice design

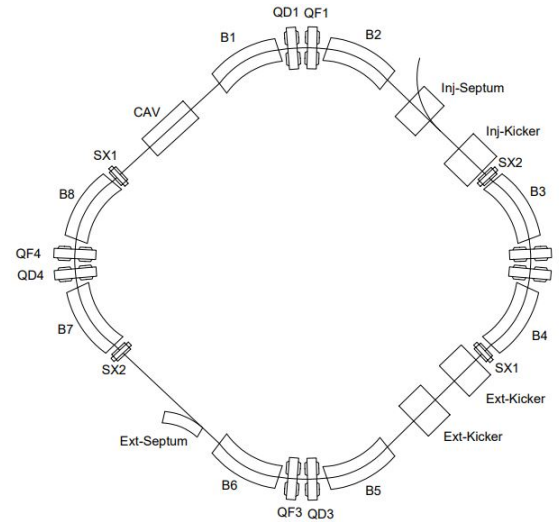


Fig. 1. Layout of the lattice design. $B(n)$ represents a dipole. $QD(n)$ and $QF(n)$ represent a defocusing quadrupole and a focusing quadrupole, respectively. Furthermore, SX1 and SX2 are two sextupole families that fit the chromaticity.

Taking into account practical considerations, such as cost and spatial limitations, the rapid cycling medical synchrotron has a lattice with a short circumference of 27.2 m, composed by four arcs and four straight sections. One straight section is used for the injection, one for the acceleration, and others for the extraction. Eight dipoles have the same length of 1.5 m and their maximum magnetic field strength are less than 1.3 T. The edge angles of dipoles are 11.25° . Eight quadrupoles, focusing in the horizontal and vertical plane,

have the same length and focusing strength. The normalized strength of defocusing quadrupoles is -2.2 and the normalized strength of focusing quadrupoles is 2 . Considering sextupolar component induced by the eddy current, two sextupole families are used to fit the chromaticity whose strengths are -15.01 and -28.42 . Figure 1 shows the layout of the lattice, where $B(n)$ represents a dipole, $QD(n)$ and $QF(n)$ represent a defocusing quadrupole and a focusing quadrupole separately, and $SX(n)$ represents a sextupole. The beta-functions and the dispersion is presented in Fig. 2 and the primary physical parameters of the synchrotron ring are listed in Table 1.

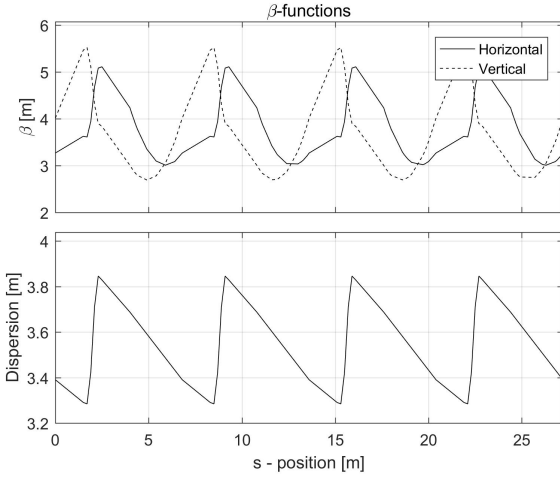


Fig. 2. Twiss parameters of the RCS. The first solid line, dotted line, and the second solid line represent horizontal betatron function, vertical betatron function, and horizontal dispersion function, respectively.

Table 1. Main parameters of RCS

| Parameters | Value |
|---|---------------|
| Ring circumference (m) | 27.2 |
| Injection energy (MeV) | 7 |
| Max.extraction energy (MeV) | 235 |
| Repetition rate (Hz) | 25 |
| Nominal tunes, H/V | 1.14/1.24 |
| Natural chromaticity | $-0.73/-0.78$ |
| The maximum beta function $\beta_x(m)/\beta_y(m)$ | 5.11 / 5.52 |
| Harmonic number | 1 |

The horizontal and vertical betatron functions were designed to be about 5 m. The horizontal dispersion function was smaller than 3.85 m. Small beta function means small beam envelope, requiring small aperture, and could realize large acceptance.

C. The injection design

Usually, there are three injection methods for synchrotron, namely the single-turn injection, the multi-turn injection and the stripping injection. Single-turn on-axis injection is simplest if could meet the particle numbers needed for the clinical treatment. A linac which can provide 7 MeV proton beams was chosen as the injector of RCS [34]. The revolution period of injection beam is 748 ns. The maximum time of single-turn on-axis injection depends on the descend time of injection element. If the injection beam current is 10 mA, this corresponds to 2.33×10^{10} protons within 374 ns, which could satisfy the requirement of 10^{10} protons per pulse. If higher particle number is required, higher injection beam current and shorter descend time of injection element is required.

The injection system is composed by a septum and a kicker. The septum is made up of a cutting plate that divides the field-free zone where the circulating beam is situated from the strong magnetic field where the injected beam is placed, therefore avoiding altering the circulating beam flow in the near area. The septum is thin enough that the injection beam stays as close to the reference orbit as feasible. The beam from the injection line is bent to a slight angle by the beam center after passing the septum. After some movement, the injection beam's trace coincides with the closed orbit, and the direction of motion has an angle. The magnetic field produced by the kicker that installed here gives the particles a kick, forcing the beam to proceed in a direction same to the closed orbit, and the beams then move in the ring along the closed orbit. After the injection, the magnetic field strength of the kicker must be promptly decreased to zero to avoid interfering with the beams that return here.

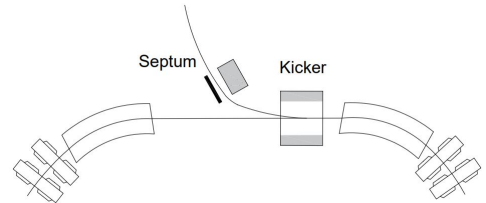


Fig. 3. Single turn injection design.

Septal and kicker parameters are listed in Table 2.

D. Extraction design

In comparison to injection, the energy of the extraction beam is higher, and the strength of the extraction components is larger. The beam extraction in the ring accelerator is much more complex. The multi-turn slow extraction is generally used in medical synchrotron for long pulse extraction beam [35]. While employing the rapid cycling synchrotron with a high repetition frequency, the beam stays at a energy for very short time. The single-turn fast extraction method is widely utilized and used in our design.

Table 2. Parameters of the injection septum and kicker

| Parameters | Septum | Kicker |
|---------------------------------|--------|--------|
| Number | 1 | 1 |
| Length (m) | 0.5 | 0.6 |
| Angle (mrad) | 430 | 37 |
| Magnetic field strength (Gauss) | 3292 | 236 |
| Decline time (ns) | | < 374 |

Here we choose a septum and two same kickers which are easy to process in reality to kick out all the beams in one turn. Placing the kickers in front of the septum could make enough space and avoid beams hitting the extraction septum. The following is a basic outline of the process: in the ring, beams are deflected by a strong magnetic field of the kicker, pass the dipole and then enter the gap of the septum. The septum bends the beams in a much larger angle to get out of the way of other components in the ring and the beams are finally transmitted to the high-energy transport line to achieve ring separation. The ramping time of the kickers must be within the time gap of the single bunch between the turn and the last turn. In the single turn rapid extraction, the extraction platform time must be sufficient to kick all the particles and the requirement for descent time is relaxed. The revolution time of the beam to be extracted depends the required energy, varies from $0.15\ \mu\text{s}$ to $0.3\ \mu\text{s}$. And the bunch length of circling beam is around 6 meters. So the rising time of kicker should be less than $0.076\ \mu\text{s}$.

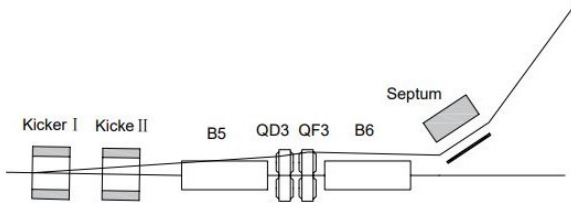


Fig. 4. Fast extraction design.

The length of the septum is 0.8 m and two kickers are 0.6 m apart. The septum is installed in another straight section. The height of the center orbit at the septum's entrance is 0.044 m and the separation height at the exit is 0.356 m. The parameters of the extraction kickers and septum are shown in Table 3.

Table 3. Parameters of the extraction septum and kickers

| Parameters | Kicker | Septum |
|---------------------------------|--------|--------|
| Number | 2 | 1 |
| Length (m) | 0.6 | 0.8 |
| Angle(mrad) | 6.5 | 180 |
| Magnetic field strength (Gauss) | 255 | 6075 |
| Rising time (ns) | <76 | |
| Septum thickness (mm) | | <3 |

III. NUMBER OF THE STORAGE PARTICLES

The beam losses are classified into two types: transverse beam losses and longitudinal beam losses. In the longitudinal direction, particles outside the RF cavity or whose momentum deviation larger than the momentum acceptance of the accelerator would lose. In the transverse direction, particles would lose if they exceed the collimator's acceptance. The stored particles' number of a low energy synchrotron is limited by space charge effects. The space charge effects occur as a result of the charged particles' electromagnetic field impacting particle movements as they pass through the accelerator. The tune shift is a parameter that represents the space charge effects. In the ring, the bucket longitudinal dimension is significantly larger than the transverse dimension. Therefore the longitudinal tune shift caused by space charge effects is several orders of magnitude smaller than the transverse tune shift. The transverse particle movements have the greater influence during the injection process. The tune shift can be described by the Eq. 1 in the situation of uniform beam distribution [36].

$$\Delta v = -\frac{N_B r_0}{2\pi \epsilon_{\text{rms}} \beta^2 \gamma^3 B_f} \quad (1)$$

where N_B is the accumulated particles, $r_0 = e^2/4\pi\epsilon_0 m_0 c^2 = 1.584 \times 10^{-18}\ \text{m}$ is for the classical proton radius, ϵ_{rms} is the transverse rms emittance about $4.1 \times 10^{-5}\ \text{mrad}$, $B_f = k_b \sigma_\sigma / \sqrt{2\pi} R$ is the bunching factor defined as the ratio of the mean to peak line charge density. When particles' number is 10^{10} , the tune shift is calculated to be approximately -0.0076 which is acceptable. The stored beam can reach 2×10^{10} or even higher. When the tune shift caused by the space charge effects leads the beam's tune to travel across the resonance line, there is a substantial chance that the particles will lose due to the resonance, resulting in a limit in the number of particles N in the ring.

To gather more particles in the ring, the space charge limit of the ring is increased as much as possible. According to

the Eq. 1, there are four ways to raise the space charge limit. One method is to increase the energy of the injected beam. One is to enhance ring acceptance and increase the size of the beams. Another method is to paint the beams evenly over the transverse phase space during the injection progress. The last one is to choose a suitable initial tune that is away from strong resonance lines.

IV. EDDY CURRENT EFFECTS

During the acceleration, the rapid varying magnetic field would induce eddy currents in vacuum chambers and other components. In turn the eddy current will generate various multipole fields which will affect beams' motion. Magnetic field attenuation and delay produced by eddy current effects impair the uniformity and synchronization of the initial magnetic field inside the vacuum chambers. Eddy current loss's thermal influence can cause temperature rise in vacuum pipes. The multipole components could cause beam tune shift and change the chromaticities. So it is necessary to consider the eddy current effect in the vacuum chambers [37].

A. Basic parameters

Eddy current effects are influenced by the hardware shape and size, material electrical conductivity, and magnetic field ramping rate. Low conductivity materials, thin pipe thicknesses, and appropriate pipe cross-section designs decrease eddy current effects in the vacuum chambers for the changing magnetic fields. According to the beam transverse envelope size, an elliptical cross-section of the vacuum chamber was chosen, where a is the vacuum chamber half-width, b is the chamber half-height, and e is the chamber thickness. To reduce the eddy current, the vacuum pipes should be made by small conductivity materials, such as ceramics. But the thickness of ceramic vacuum pipe is too high and increase the magnet gap and power very much. A low conductivity material Inconel 625 is used [38]. The ramping is realized by

Table 4. Sectional size of the vacuum chamber

| a (mm) | b (mm) | e (mm) | Material | σ (S/m) |
|-------------|-------------|-------------|-------------|-------------------|
| 25 | 19 | 0.3 | Inconel 625 | 0.8×10^6 |

improving the strength of the dipoles and quadrupoles.

For a sinusoidal ramp, the time variation of the dipole magnetic field is provided by Eq. 2 [39]

$$B(t) = B_0 [a_1 - \cos(2\pi f_r t)], \quad (2)$$

where $B_0 = (B_{\max} - B_{\min})/2$, $a_1 = (B_{\max} + B_{\min})/(B_{\max} - B_{\min})$, and f_r is the repetition rate.

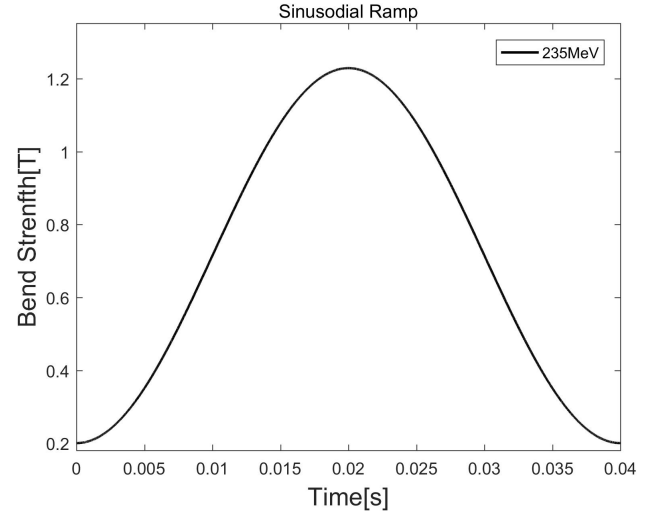


Fig. 5. Sinusoidal ramping curve for the dipole field.

The minimum dipole strength is 0.20038 T when injected, and the maximum is 1.2294 T when extracted. Figure 5 illustrates the ramping curve of the dipole field.

B. Induced sextupolar component in the dipoles chambers

The eddy current magnetic field within the vacuum chamber of the dipoles has a significant impact on the dipole component, leading to magnetic field attenuation and delay. Concurrently, the sextupolar component of the eddy-current magnetic field in the dipole vacuum chamber induces changes in chromaticities. Additionally, the quadrupole component of the eddy-current magnetic field in the vacuum chamber of the quadrupole magnet section results in a lateral tune shift.

The formula for the sextupolar component in elliptical vacuum chambers can be expressed by Eq. 3[39] as follows:

$$m_3 = \frac{\mu_0 \sigma e}{h} \frac{\dot{B}}{B\rho} J \quad (3)$$

where $\sigma = 0.8 \times 10^6$ S/m denotes the electrical conductivity of Inconel 625. Furthermore, $\mu_0 = 4\pi \times 10^{-7}$ denotes vacuum permeability, ρ denotes the dipole bending radius, \dot{B} denotes the rate of change in the field, and J denotes the geometric factor of the elliptical vacuum chamber.

$$J = \int_0^{\pi/2} \sin \varphi \sqrt{\cos^2 \varphi + \left(\frac{b}{a}\right)^2 \sin^2 \varphi} d\varphi$$

where a denotes the vacuum chamber half-width and b denotes the half-height of the chamber.

The sextupole strength introduced during the sinusoidal ramping is shown in Fig. 6. When $t = 5.0$ ms, the sextupolar exhibits a maximum value of 1.143 m^{-3} . This is also verified in Opera software's ELEKTRA module as shown in Fig. 7. The geometrical factors and B'/B are related to the strength of the eddy current magnetic field's sextupole component.

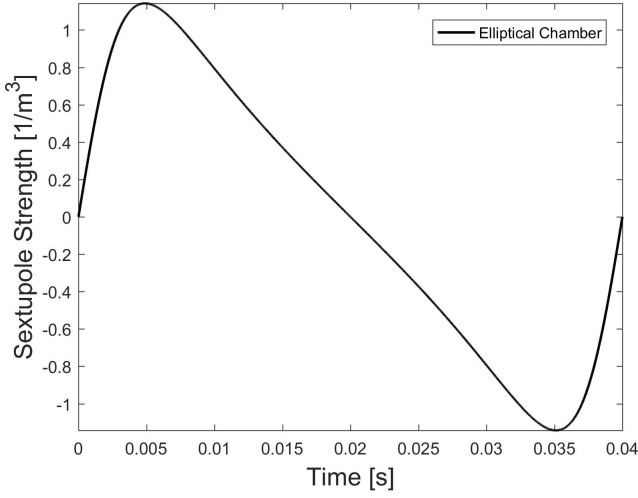


Fig. 6. Sextupole strength introduced by the sinusoidal ramping curve.

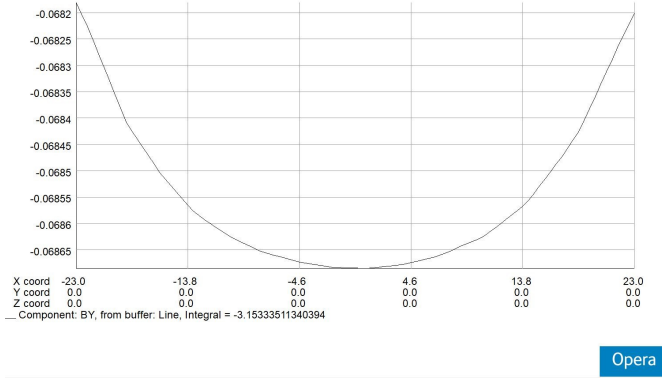


Fig. 7. When $t=0.01$ s, the magnetic center plane is distributed along line $x = -23$ mm to $x = 23$ mm.

The sextupolar component induced by eddy currents is calculated as the sextupole component errors of dipoles, and causes horizontal and vertical chromaticity modification described by $\varepsilon_{x,co}$ and $\varepsilon_{y,co}$.

$$\begin{cases} \varepsilon_{x,co} = \varepsilon_{x,0} + \Delta\varepsilon_z = -0.73 + 31.03m_3 \\ \varepsilon_{y,co} = \varepsilon_{y,0} + \Delta\varepsilon_y = -0.78 - 27.27m_3 \end{cases} \quad (4)$$

The maximum horizontal chromaticity is $\varepsilon_{x,co} = 34.74$, and the minimum vertical chromaticity is $\varepsilon_{y,co} = -31.95$. Because of chromaticity changes caused by the sextupole component of the eddy current effects, the transverse working tune may change and cross the resonance line. When designing beam optics, it is necessary to consider the errors introduced by the sextupole component, chromaticity correction should be done in the ramping. Two sextupole families are used to fit the chromaticity to the value of 0.5 and 0.5 in the horizontal and vertical direction.

C. Induced dipole component in the dipoles chambers

The dipole component can also be induced by eddy currents in the dipole vacuum chamber. This can be described by Eq. 5 [40] as follows:

$$m_1 = \frac{-\mu_0 \sigma e \dot{B} F}{2\pi \rho B h}, \quad (5)$$

$$F = \pi \left(\frac{a_2^2 b_2}{a_2 + b_2} - \frac{a_1^2 b_1}{a_1 + b_1} \right),$$

where a_1 , a_2 , b_1 , and b_2 denote the vacuum chambers inside the half-width, outside half-width, inside half-height, and outside half-height, respectively. Maybe the presence of the vacuum box could cause the effect of magnetic stranded for the RCS, with a time constant of $3.5254 \mu\text{s}$. This is acceptable. Figure 8 shows the acceptable effects of magnetic stranded for the sinusoidal ramping within 0.04 s.

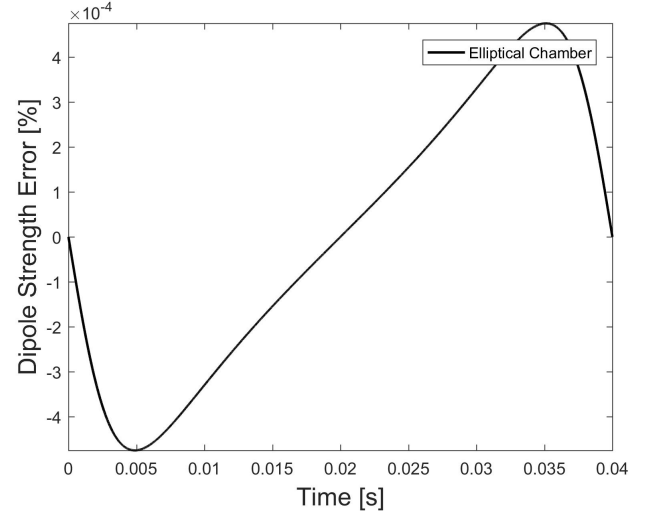


Fig. 8. Dipole strength errors introduced by the sinusoidal ramping curve.

D. Induced quadrupolar component in the quadrupole vacuum chamber

Similar to the dipole vacuum chamber, eddy current effects exist, and only the quadrupolar component would be generated. For a circular vacuum chamber of \bar{r} medium radius, the quadrupolar strength is given by Eq. 6[39]

$$m_2 = -\frac{7}{16} \mu_0 \sigma e \bar{r} \times \frac{\dot{B}}{B \rho}. \quad (6)$$

Figure 9 shows that the magnetic hysteresis induced by the quadrupolar component in the vacuum chamber is small. As shown in Fig. 10, the maximum tune shift introduced by the quadrupolar component is within 4×10^{-4} .

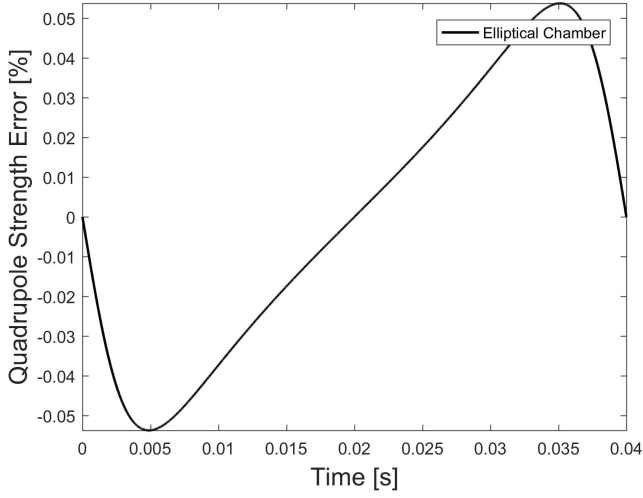


Fig. 9. Quadrupole strength errors introduced by the sinusoidal ramping curve.

Compared to the initial transverse tune, the transverse tune shift due to the quadrupole component of the eddy-current magnetic field is significantly less than the error introduced by the quadrupole magnet.

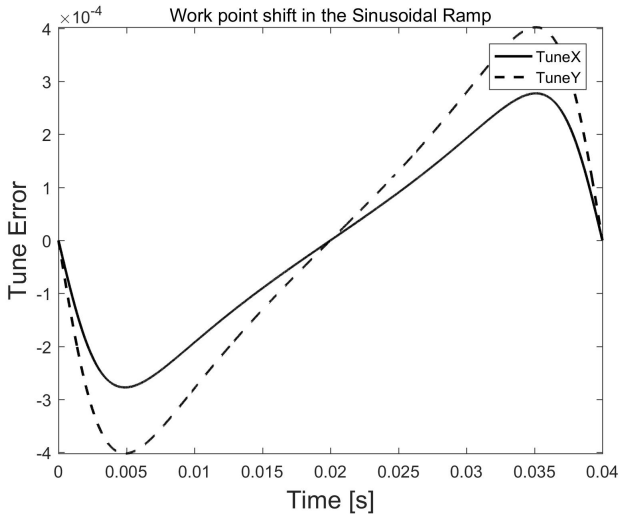


Fig. 10. Horizontal and vertical tune shifts introduced by quadrupolar component.

E. Power loss introduced by eddy currents in the vacuum chamber

The existence of electrical resistance would lead to heating effects. When the vacuum chamber is heated to a high temperature for a long time, the vacuum inside the chamber would decrease. In an extremely high vacuum environment, the gas molecules adsorbed on the vacuum chamber wall ab-

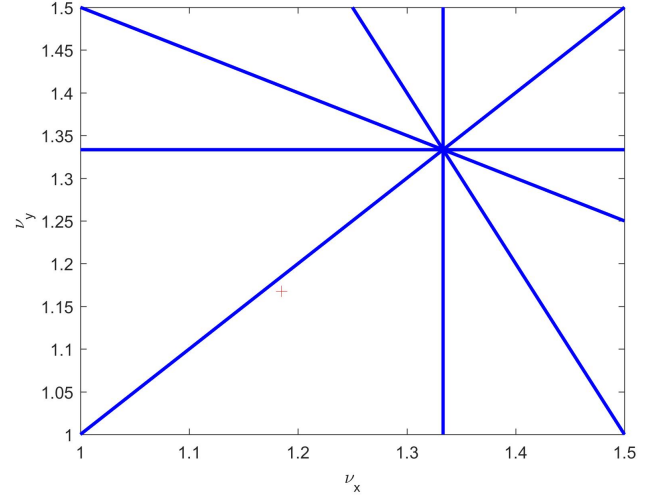


Fig. 11. Resonance line diagram.

sorb heat and diffuse into the vacuum chamber. Then the vacuum would decrease and the beam lifetime would shorten. From an engineering point of view, overheated tube temperatures can cause aging and cracking of the epoxy resin in the dipole magnet core. Generally speaking, the temperature of the vacuum chamber does not exceed 80 °C. The eddy current power loss per unit length is given by Eq. 7 and is shown in Fig. 12[41].

$$\frac{P_{\text{eddy}}}{L} = 4\sigma \dot{B}^2 e a^3 \times H \quad (7)$$

where

$$H = \int_0^{\pi/2} \sin^2 \varphi \sqrt{\cos^2 \varphi + \left(\frac{b}{a}\right)^2 \sin^2 \varphi} d\varphi$$

where a , b , h are the vacuum chamber half-width, vacuum chamber half-height and magnet gap half-height. To visualize the effect of power loss on the vacuum chamber we perform a transient EMF research using the ELEKTRA TR module in Opera software and calculated eddy current loss distribution. The eddy current loss is proportional to the magnetic field rate of change squared. The rate of change of the magnetic field in a single cycle is not constant. In the eddy current loss thermal analysis, the average eddy current loss in a single cycle is used and the average eddy current loss factor is 0.6434 by averaging and integrating the values over a time period. Then we create a static thermal analysis model in Opera software's TEMPO ST module. The thermal conductivities of the magnet core and Inconel 625 is shown in Table 5. The exterior surface of the vacuum chamber is configured for heat dissipation by air convection and the heat transfer coefficient is 14 W/(m² · K). The initial ambient temperature is 28 °C.

We multiplied the average eddy current loss factor of 0.6434 by the eddy current loss distribution of the vacuum chamber under changing magnetic fields derived from the ELEKTRA TR module's eddy current effect simulation. We

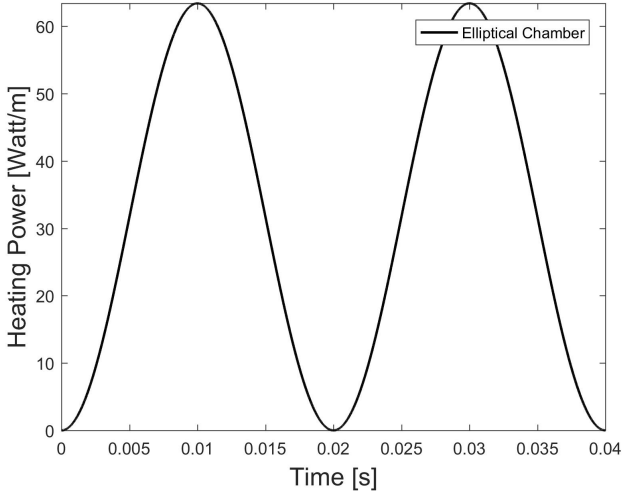


Fig. 12. Eddy current power loss per unit length.

Table 5. Thermal conductivities

| Thermal conductivity | Magnet core | Inconel 625 |
|----------------------|-------------|-------------|
| X (W/(m · K)) | 28 | 12.1 |
| Y (W/(m · K)) | 28 | 12.1 |
| Z (W/(m · K)) | 0.37 | 12.1 |

imported it as a steady-state heat source distribution into the vacuum chamber model in the TEMPO ST module. After simulation the temperature distribution of the chamber after the eddy current loss is depicted in Fig. 13.

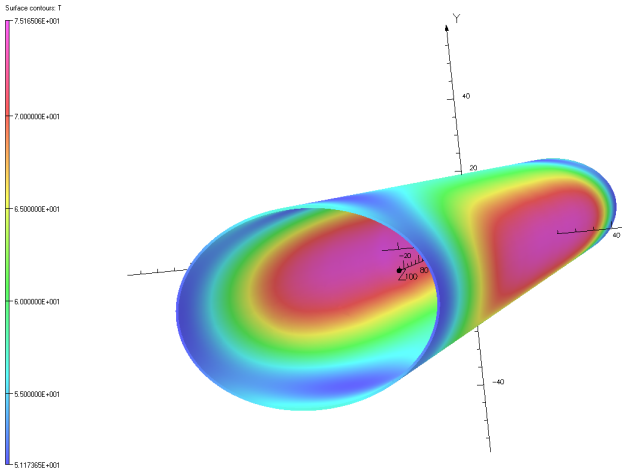


Fig. 13. (Color online) Temperature distribution of the thick vacuum chamber after eddy current loss temperature rise.

The power losses at vacuum chamber was 23.63 W, and we can observe from the picture that the highest temperature is 75.165 °C within acceptable limits for engineering applica-

tions. This result is very close to the theoretical result.

V. ENERGY SWITCHING

Multiple energy extraction will be required for FLASH proton transport. Because the beam can be extracted from the ring in a single turn, compared to the time of a cycle, the extraction time can be neglected and also the injection. Its energy may be easily altered from one cycle to the next.

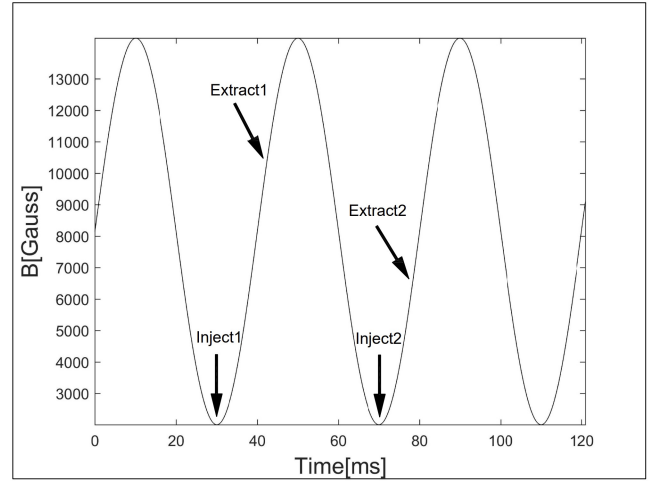


Fig. 14. Variation of magnetic field with time.

Three magnetic field cycles of the RCS are shown in Fig. 14. Beam is injected at the bottom('inject 1' and 'inject 2'). The beam is extracted at the different position of the cycle to obtain different energy levels ('extract 1' and 'extract 2'). The magnetic field cycle remained constant to reduce the hysteresis effect and control difficulty. The only change is the delay between the injection and extraction, with the strength of extraction element [42]. The frequency and voltage of the RF vary according to the energy.

VI. CONCLUSION

Currently it is still challenging to improve accelerator technology to implement proton FLASH therapy. We propose a novel design for proton FLASH therapy using a rapid-cycling synchrotron. In our design, The lattice, injection, extraction, space charge effects, eddy current effects and rapid energy switching are considered. The RCS can provide 10^{10} protons/pulse. The irradiation time of a 60 Gray plan is about 1 min and the instantaneous dose rate could reach 10^7 Gy/s. Compared to laser plasma accelerator or slow extraction synchrotron, this is a cheap and simple design. If higher dose rate is required, the beam intensity of a spill can be increased.

AUTHOR CONTRIBUTIONS

All authors contributed to the study conception and design. Material preparation, data collection and analysis were performed by Ying Shi, and Man-Zhou Zhang. The first draft of the manuscript was written by Ying Shi and all authors commented on previous versions of the manuscript. All authors read and approved the final manuscript. The software use was helped by Lian-Hua Ou-Yang. And the article was supervised and revised by Man-Zhou Zhang, Zhi-Ling Chen, Xiu-Fang Li and De-Ming Li.

DATA AVAILABILITY STATEMENT

The data that support the findings of this study are openly available in Science Data Bank at <https://doi.org/10.57760/sciencedb.j00186.00169> and <https://cstr.cn/31253.11.sciencedb.j00186.00169>.

CONFLICT OF INTEREST

Man-Zhou Zhang is an editorial board member for Nuclear Science and Techniques and was not involved in the editorial review, or the decision to publish this article. All authors declare that there are no competing interests.

- [1] V. Favaudon, L. Caplier, V. Monceau, et al., Ultrahigh dose-rate flash irradiation increases the differential response between normal and tumor tissue in mice. *Sci. Transl. Med.* **6**, 9 (2014). doi:10.1126/scitranslmed.3008973
- [2] J.D. Wilson, E.M. Hammond, G.S. Higgins, et al., Ultra-high dose rate (flash) radiotherapy: Silver bullet or fool's gold? *Front. Oncol.* **9**, 12 (2020). doi:10.3389/fonc.2019.01563
- [3] H. Zhu, D. Xie, Y. Yang, et al., Radioprotective effect of x-ray abdominal flash irradiation: Adaptation to oxidative damage and inflammatory response may be benefiting factors. *Med. Phys.* **49**, 4812–4822 (2022). doi:10.1002/mp.15680
- [4] P. Montay-Gruel, A. Bouchet, M. Jaccard, et al., X-rays can trigger the flash effect: Ultra-high dose-rate synchrotron light source prevents normal brain injury after whole brain irradiation in mice. *Radiother. Oncol.* **129**, 582–588 (2018). doi:10.1016/j.radonc.2018.08.016
- [5] E. Schüller, S. Trovati, G. King, et al., Experimental platform for ultra-high dose rate flash irradiation of small animals using a clinical linear accelerator. *Int. J. Radiat. Oncol.* **97**, 195–203 (2017). doi:10.1016/j.ijrobp.2016.09.018
- [6] P. Montay-Gruel, M.M. Acharya, K. Petersson, et al., Long-term neurocognitive benefits of flash radiotherapy driven by reduced reactive oxygen species. *P Natl. Acad. Sci. USA* **116**, 10943–10951 (2019). doi:10.1073/pnas.1901777116
- [7] T.F. Rösch, Z. Szabó, D. Haffa, et al., A feasibility study of zebrafish embryo irradiation with laser-accelerated protons. *Rev. Sci. Instrum.* **91**, 8 (2020). doi:10.1063/5.0008512
- [8] E. Beyreuther, M. Brand, S. Hans, et al., Feasibility of proton flash effect tested by zebrafish embryo irradiation. *Radiother. Oncol.* **139**, 46–50 (2019). doi:10.1016/j.radonc.2019.06.024
- [9] M.C. Vozenin, P. De Fornel, K. Petersson, et al., The advantage of flash radiotherapy confirmed in mini-pig and cat-cancer patients. *Clin. Cancer. Res.* **25**, 35–42 (2019). doi:10.1158/1078-0432.Ccr-17-3375
- [10] J. Bourhis, W.J. Sozzi, P.G. Jorge, et al., Treatment of a first patient with flash-radiotherapy. *Radiother. Oncol.* **139**, 18–22 (2019). doi:10.1016/j.radonc.2019.06.019
- [11] S. Wei, C. Shi, C.C. Chen, et al., Recent progress in pencil beam scanning flash proton therapy: a narrative review. *Ther. Radiol. Oncol.* . doi:dx.10.21037/tro-22-1
- [12] S. Van De Water, S. Safai, J.M. Schippers, et al., Towards flash proton therapy: the impact of treatment planning and machine characteristics on achievable dose rates. *ACTA. Oncol.* **58**, 1463–1469 (2019). doi:10.1080/0284186X.2019.1627416
- [13] M. Kang, S. Wei, J.I. Choi, et al., Quantitative assessment of 3d dose rate for proton pencil beam scanning flash radiotherapy and its application for lung hypofractionation treatment planning. *Cancers* **13**, 3549 (2021). doi:10.3390/cancers13143549
- [14] P. van Marlen, M. Dahele, M. Folkerts, et al., Bringing flash to the clinic: Treatment planning considerations for ultrahigh dose-rate proton beams. *Int. J. Radiat. Oncol. Biol. Phys.* **106**, 621–629 (2020). doi:INT J RADIAT ONCOL
- [15] M. Krieger, S. van de Water, M.M. Folkerts, et al., A quantitative flash effectiveness model to reveal potentials and pitfalls of high dose rate proton therapy. *Med. Phys.* **49**, 2026–2038 (2022). doi:10.1002/mp.15459
- [16] G. Adrian, E. Konradsson, M. Lempart, et al., The flash effect depends on oxygen concentration. *Brit. J. Radiol.* **93**, 20190702 (2020). doi:10.1259/bjr.20190702
- [17] P. Wilson, B. Jones, T. Yokoi, et al., Revisiting the ultra-high dose rate effect: implications for charged particle radiotherapy using protons and light ions. *Brit. J. Radiol.* **85**, e933–9 (2012). doi:10.1259/bjr/17827549
- [18] H. Gao, J. Liu, Y. Lin, et al., Simultaneous dose and dose rate optimization (sddro) of the flash effect for pencil-beam-scanning proton therapy. *Med. Phys.* **49**, 2014–2025 (2022). doi:10.1002/mp.15356
- [19] Z. Mei, Y. Yuan, J. Wang, et al., Focused proton beam generating pseudo bragg peak for flash therapy. *Nucl. Instrum. Meth. A* **1032**, . doi:10.1016/j.nima.2022.166618
- [20] J. Bin, L. Obst-Huebl, J.H. Mao, et al., A new platform for ultra-high dose rate radiobiological research using the bella pw laser proton beamline. *Sci. Rep-UK.* **12**, 1484 (2022). doi:10.1038/s41598-022-05181-3
- [21] S. Boucher, E. Esarey, C. Geddes, et al., Transformative technology for flash radiation therapy: A snowmass 2021 white paper. arXiv preprint arXiv:2203.11047 .
- [22] L. Labate, D. Palla, D. Panetta, et al., Toward an effective use of laser-driven very high energy electrons for radiotherapy: Feasibility assessment of multi-field and intensity modulation irradiation schemes. *Sci. Rep-UK* **10**, 11 (2020). doi:10.1038/s41598-020-74256-w
- [23] S. Auer, V. Hable, C. Greubel, et al., Survival of tumor cells after proton irradiation with ultra-high dose rates. *RADIAT. ONCOL.* **6**, 139 (2011). doi:10.1186/1748-717X-6-139
- [24] G. Aymar, T. Becker, S. Boogert, et al., Lhara: The laser-hybrid accelerator for radiobiological applications. *Front. Phys.-LAUSANNE* **8**, 21 (2020). doi:10.3389/fphy.2020.567738

- [25] J. Bin, K. Allinger, W. Assmann, et al., A laser-driven nanosecond proton source for radiobiological studies. *Appl. Phys. Lett.* **101**, 4 (2012). doi:10.1063/1.4769372
- [26] S. Jolly, H. Owen, M. Schippers, et al., Technical challenges for flash proton therapy. *Phys. Medica* **78**, 71–82 (2020). doi:10.1016/j.ejmp.2020.08.005
- [27] E.S. Diffenderfer, I.I. Verginadis, M.M. Kim, et al., Design, implementation, and in vivo validation of a novel proton flash radiation therapy system. *Int. J. Radiat. Oncol.* **106**, 440–448 (2020). doi:10.1016/j.ijrobp.2019.10.049
- [28] A. Patriarca, C. Fouillade, M. Auger, et al., Experimental set-up for flash proton irradiation of small animals using a clinical system. *Int. J. Radiat. Oncol.* **102**, 619–626 (2018). doi:10.1016/j.ijrobp.2018.06.403
- [29] W.C. Fang, X.X. Huang, J.H. Tan, et al., Proton linac-based therapy facility for ultra-high dose rate (flash) treatment. *Nucl. Sci. Tech.* **32**, 9 (2021). doi:10.1007/s41365-021-00872-4
- [30] Y. Zhang, W.C. Fang, X.X. Huang, et al., Design, fabrication, and cold test of an s-band high-gradient accelerating structure for compact proton therapy facility. *Nucl. Sci. Tech.* **32**,. doi:10.1007/s41365-021-00869-z
- [31] Y.Q. Yang, W.C. Fang, X.X. Huang, et al., Static superconducting gantry-based proton ct combined with x-ray ct as prior image for flash proton therapy. *Nucl. Sci. Tech.* **34**,. doi:10.1007/s41365-022-01163-2
- [32] L.M. Smyth, J.F. Donoghue, J.A. Ventura, et al., Comparative toxicity of synchrotron and conventional radiation therapy based on total and partial body irradiation in a murine model. *Sci. Rep.-UK* **8**, 12044 (2018). doi:10.1038/s41598-018-30543-1
- [33] S. Kraft, C. Richter, K. Zeil, et al., Dose-dependent biological damage of tumour cells by laser-accelerated proton beams. *New. J. Phys.* **12**, 12 (2010). doi:10.1088/1367-2630/12/8/085003
- [34] X. Li, Y.H. Pu, F. Yang, et al., Rf design and study of a 325 mhz 7 mev apf ih-dtl for an injector of a proton medical accelerator. *Nucl. Sci. Tech.* **30**, 135 (2019). doi:10.1007/s41365-019-065-4
- [35] Y.H. Yang, M.Z. Zhang, D.M. Li, Simulation study of slow extraction for the shanghai advanced proton therapy facility. *Nucl. Sci. Tech.* **28**, 7 (2017). doi:10.1007/s41365-017-0273-0
- [36] M. Ferrario, M. Migliorati, L. Palumbo, Space charge effects. CERN-2014/009. doi:10.5170/CERN-2014-009.331
- [37] M.Z. Zhang, M. Zhang, X.C. Xie, et al., Eddy current effects in a high field dipole. *Nucl. Sci. Tech.* **28**, 6 (2017). doi:10.1007/s41365-017-0325-5
- [38] S.Y. Xu, S. Wang, Study of eddy current power loss in an rcs vacuum chamber. *Chinese. Phys. C* **36**, 160–166 (2012). doi:10.1088/1674-1137/36/2/011
- [39] A. Lachaize, Estimate of eddy current effects in the vacuum chamber of the beta-beam rcs. . doi:https://cds.cern.ch/record/1355340
- [40] N.S. Sereno, S.H. Kim, Eddy-current-induced multipole field calculations. Report, Argonne National Lab., IL (US) (2003). doi:10.2172/816760
- [41] G. Hemmie, J. Rossbach, Eddy current effects in the desy ii dipole vacuum chamber. Report (1984)
- [42] D. Trbojevic, J. Alessi, M. Blaskiewicz, et al., Lattice design of a rapid cycling medical synchrotron for carbon/proton therapy. Proceedings of IPAC, 2011 WEPS028 (2011).